Examining Recrystallization During Hot Rolling of HSLA Steels Using Gleeble Hot Torsion






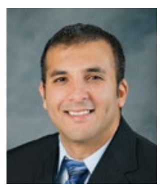


Motivated by inconsistencies in low-temperature toughness of nominally identical hot-rolled high-strength, low-alloy (X65-80) strip, the present study utilizes Gleeble hot torsion simulation to examine thermomechanical processing effects. Recrystallization characteristics of rolled and simulated microstructures were compared using electron backscatter diffraction, with specific toughness-relevant texture components isolated from resultant orientation distribution function maps. Given the importance of controlling austenite recrystallization, temperature ranges for full, partial and negligible recrystallization were measured using double-twist Gleeble testing. After establishing baseline ranges for fully annealed material, the accumulated effects of hot rolling passes were examined through iteratively incorporating reduction passes prior to subsequent double-twist testing.

Authors

Shiraz Mujahid (top left), Research Engineer, Center for Advanced Vehicular Systems, Mississippi State University, Starkville, Miss., USA
shiraz@cavs.msstate.edu

Dawn Van Iderstine (top center), Research Engineer, Center for Advanced Vehicular Systems, Mississippi State University, Starkville, Miss., USA
dv291@cavs.msstate.edu

Dmitry Tsvetkov (top right), Hot Mill Metallurgist, Steel Dynamics Inc. – Flat Roll Group Southwest-Sinton Division, Sinton, Texas, USA
dmitry.tsvetkov@steeldynamics.com

Jonathan Becerril (middle left), Hot Mill Product Metallurgist, Steel Dynamics Inc. – Flat Roll Group Columbus Division, Columbus, Miss., USA
jonathan.becerril@steeldynamics.com

C. Matthew Enloe (middle center), Quality and Product Development Manager, Steel Dynamics Inc. – Flat Roll Group Southwest-Sinton Division, Sinton, Texas, USA
matt.enloe@steeldynamics.com

Haitham El Kadiri (middle right), Director and Professor, Michael W. Hall School of Mechanical Engineering, Mississippi State University, Mississippi State University, Starkville, Miss., USA
elkadiri@me.msstate.edu

Hongjoo Rhee (bottom), Senior Associate Director, Center for Advanced Vehicular Systems; and Professor, Michael W. Hall School of Mechanical Engineering, Mississippi State University, Mississippi State University, Starkville, Miss., USA
hrhee@me.msstate.edu

Introduction

Thermomechanical-controlled processing (TMCP) strategies for steel production utilize hot deformation (e.g., hot rolling) to achieve combined outcomes for shape (thickness, flatness, etc.) as well as microstructure and properties (strength, ductility, toughness) through intricate control of process parameters. TMCP methods offer significant cost savings for a wide range of products, including line pipe, construction, automotive and shipbuilding.[1]

To promote uniformly refined microstructures, TMCP schedules employ two stages during production. In the first stage, deformations are applied at high enough temperatures to induce full recrystallization into small, uniform austenite grains. As temperatures decrease and recrystallization halts, the second stage involves reaching final product dimensions while deforming, or "pancaking," the refined austenite. Higher dislocation densities in pancaked austenite promote nucleation of refined ferrite with favorable crystallographic textures during cooling.[2–4]

High-temperature microstructure evolution during TMCP is complex, owing to the interdependence of processing parameters such as deformation, deformation rate, temperature and time at industrial production scales.[5,6] Physical simulation using Gleeble hot torsion as a surrogate for hot rolling enables in-depth examination of the process and outcome with relatively precise and independent control of each of the relevant processing parameters.[7–12]

Figure 1

Discrepant Charpy behavior at multiple temperatures, with orientation of Charpy samples in rolled plate.

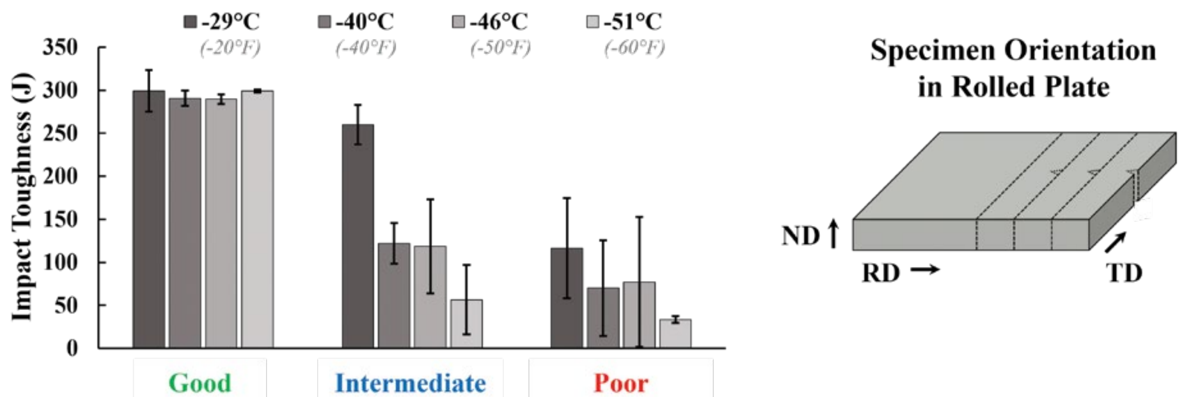

Table 1

Compositions of Steels (wt. %) Along With A_3 Temperatures (°C)

	C	Mn	Si	P	S	Cu+Ni+Mo+Cr	Al	B	Nb+V+Ti	Ca	N	A_3
Good	0.05	1.15	0.20	0.010	0.002	0.21	0.027	0.0003	0.085	0.001	0.008	859
Intermediate/ Poor	0.05	1.20	0.20	0.008	0.002	0.20	0.026	0.0003	0.085	0.002	0.008	857

Motivation

The present study was prompted by the observation that nominally identical commercially produced Nb+V+Ti X65 steel coils exhibited inconsistent Charpy performance despite no discernible inconsistency in other physical metrics. While this inconsistency was seen across numerous coils, three particular coils were chosen for this study, henceforth designated "good," "intermediate" and "poor" based on their Charpy performance, shown in Fig. 1. The good coil showed consistently high toughness over a wide range of temperatures with minimal variability (shown by sizes of error bars). By comparison, the toughness of the poor material was markedly lower, accompanied by significantly greater variability. The intermediate material showed reasonable toughness at –29°C (–20°F) but descended to similar behavior as the poor material at colder temperatures.

The chemical compositions of the three coils were very similar, as shown in Table 1, with the intermediate and poor coils sharing identical composition as a result of both being produced from the same heat. The upper critical temperatures, A_3, were also determined by CALPHAD (calculation of phase diagrams) using Thermo-Calc 2020a.[13]

Figure 2

Average strength (yield = YS, ultimate tensile = UTS) and elongation (uniform = UE, total = TE) of each coil.

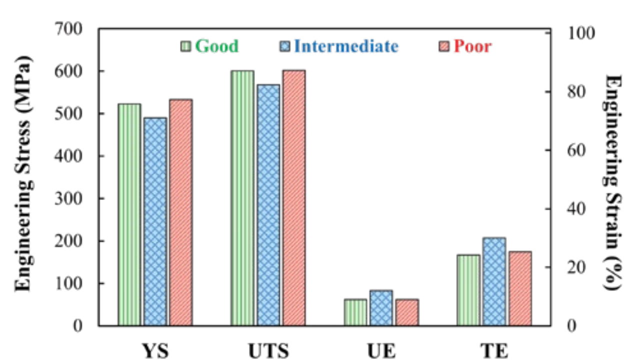

Despite the pronounced variability in impact behavior, quasi-static tensile performance (Fig. 2) was relatively consistent across all three coils and did not follow the significant trend displayed by the Charpy results.

The lack of significant variability under quasi-static tension prompted the examination of strain rate effects,

Figure 3

High-strain-rate behavior (400/second) along the rolling direction (RD) and transverse direction (TD).

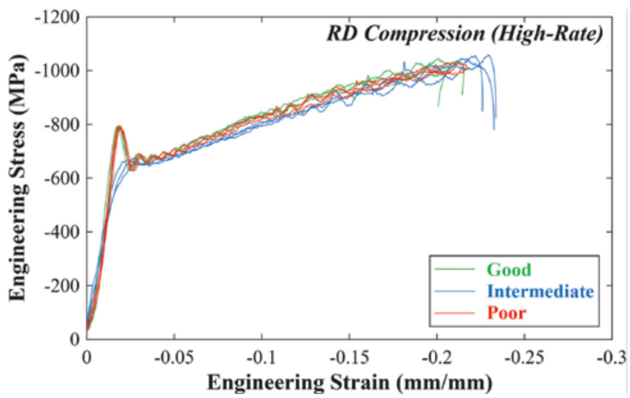

since Charpy impact tests have been shown to occur in the range of 10^2/second to 10^3/second.[14–16] Test specimens were extracted from the plate material with deformation axes along the rolling (longitudinal) and transverse (long transverse) directions and subjected to high-rate compression at 400/second using a split Hopkinson pressure bar. The results (Fig. 3) present no discernible trend in high-rate behavior across the three coils to echo the discrepancy in their Charpy performances.

Following the process-structure-property hierarchy of materials development, the causes for inconsistencies in material properties were investigated through analysis of the manufacturing process and the resulting microstructures.

Analysis of Processing History

The steel coils were produced on a CSP rolling mill using the following technological operations: continuous slab casting, subsequent reheating to the specified rolling temperatures, hot rolling according to TMCP strategy on a 6-stand finishing mill (designated F1–F6), and cooling on a reinforced laminar cooling system. The rolling strategy targeted austenite recrystallization for grain refinement in F1 and F2, followed by deformation, or pancaking, of recrystallized austenite across F3–F6 for toughness.[3,4] Production logs were analyzed for differences between processing routes, particularly temperature vs. rolling stand and temperature vs. time (Fig. 4). Initial examination revealed that the good coil had the fastest processing time by a considerable margin. By contrast, the poor coil consistently had the lowest temperature at each stand as well as the slowest processing speed. The intermediate coil had similar reduction temperatures as the good coil but similar processing speeds as the poor coil.

To gain some insight on thermal history effects in the context of phase transformations, time-temperature-transformation (TTT) profiles for the three coils were generated by CALPHAD methods using JMatPro.[17] Since the austenite grain size prior to hot rolling is not precisely known, JMatPro hot rolling simulations based on rolling profiles from mill logs for each coil were used to determine grain sizes for TTT calculation inputs. Despite testing a large range of initial austenite grain sizes (500–2,000 µm), JMatPro simulations showed that

Figure 4

Thermal processing history of each coil plotted against rolling stand (left) and time (right).

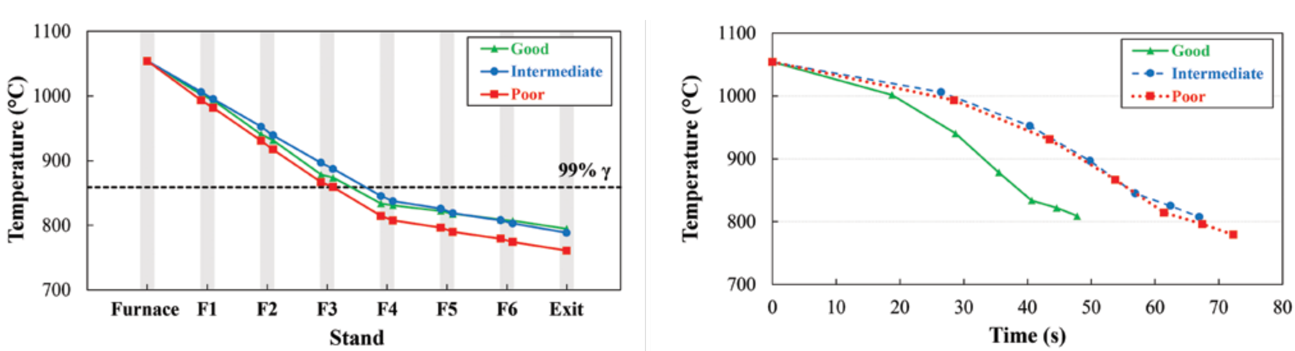

Figure 5

Rolling histories overlaid on time-temperature-transformation profiles. Figures in the bottom row show the last three rolling reductions relative to phase transformation thresholds for good, intermediate and poor coils (left to right).

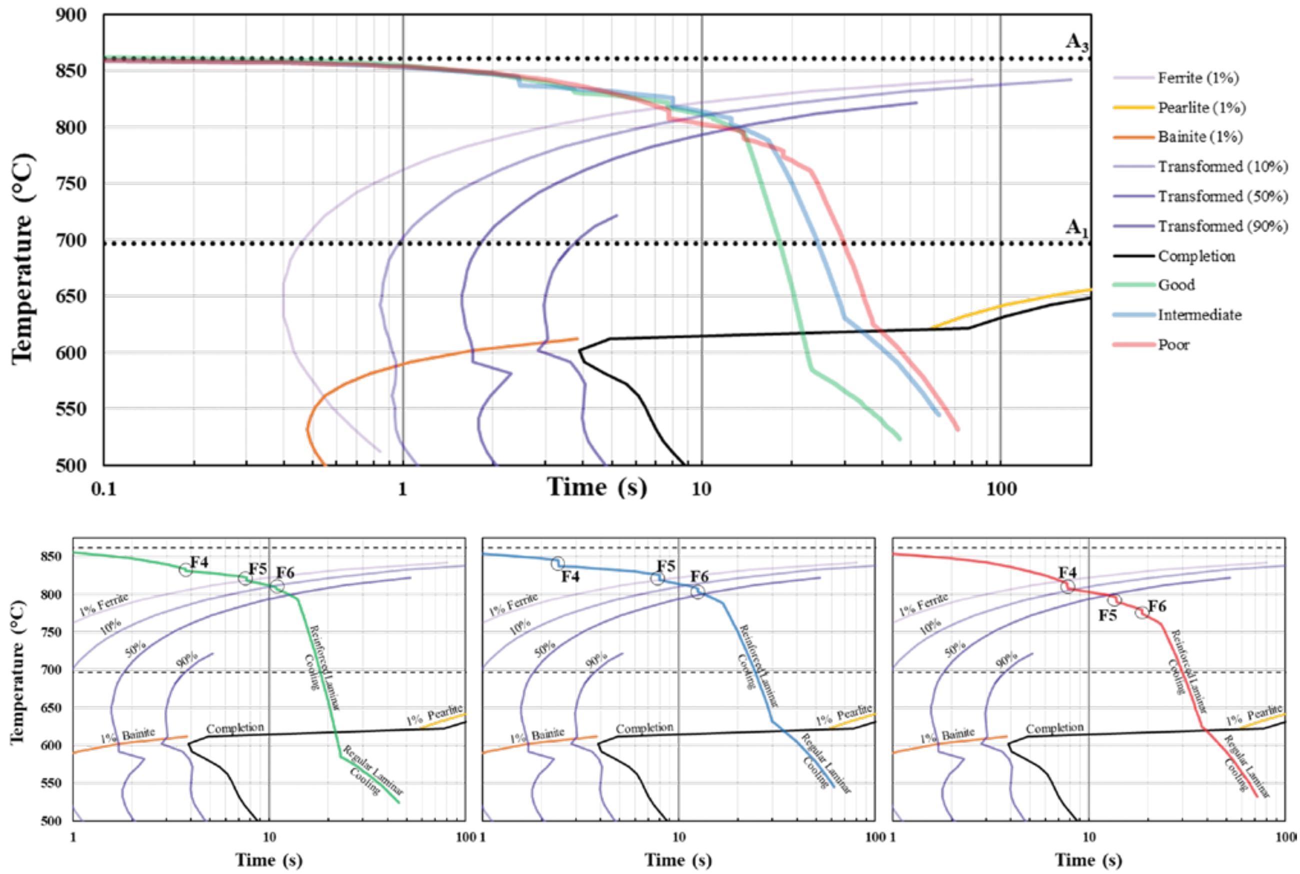

the grain sizes consistently converged to very similar values after F3. Additionally, the temperature of each coil dropped below A_3 between stands 3 and 4. Thus, the simulated grain sizes after F3 (42 µm for good, 43 µm for intermediate, 41 µm for poor) were used to calculate the TTT diagram for each coil.

To overlay thermal profiles with TTT curves (Fig. 5), start time was set at 0.1 second after dropping below A_3 (since 0 seconds cannot be accommodated on the logarithmic time axis). The good and intermediate coils undergo complete reduction at F4 and near-complete reduction at F5 prior to reaching the ferrite transformation nose. Furthermore, by the time the last reduction at F6 is finished, the thermal profiles are barely past the 10% transformation nose. Thus, F4 and F5 deformations take place while the material is estimated to be entirely austenitic, with the F6 pass occurring on up to 90% untransformed austenite fraction. In contrast, the poor coil experienced F4 after reaching the ferrite nose, with reductions at F5 and F6 occurring after over 50% of austenite had already transformed into ferrite. The combination of slower line speed and faster temperature drop for the poor coil results in the last three reductions being applied to a mostly ferritic microstructure, rather than the more favorable pancaking of austenite.

Microstructure Analysis

To observe the microstructures within each coil, samples were sectioned from the Charpy specimens prior to mounting and polishing. Initial optical metallography (2% Nital etch) revealed mixed microstructures, with refined grains interspersed among large, coarse grains elongated along rolling direction, shown in Fig. 6. The coarse grains were larger in the intermediate and poor samples and could be indicative of inconsistent recrystallization during processing. These mixed microstructures have been shown to negatively affect the impact properties of steels.[18–20]

While optical metallography is instructive, the imaged microstructures occur after rolling, cooling and transformation. Deeper analysis of the microstructure was performed in an attempt to back-solve for events which occurred upstream during processing. The etched samples were repolished to a 40 nm colloidal silica surface

Figure 6

Optical metallography images highlighting coarse and refined microstructures in each coil.

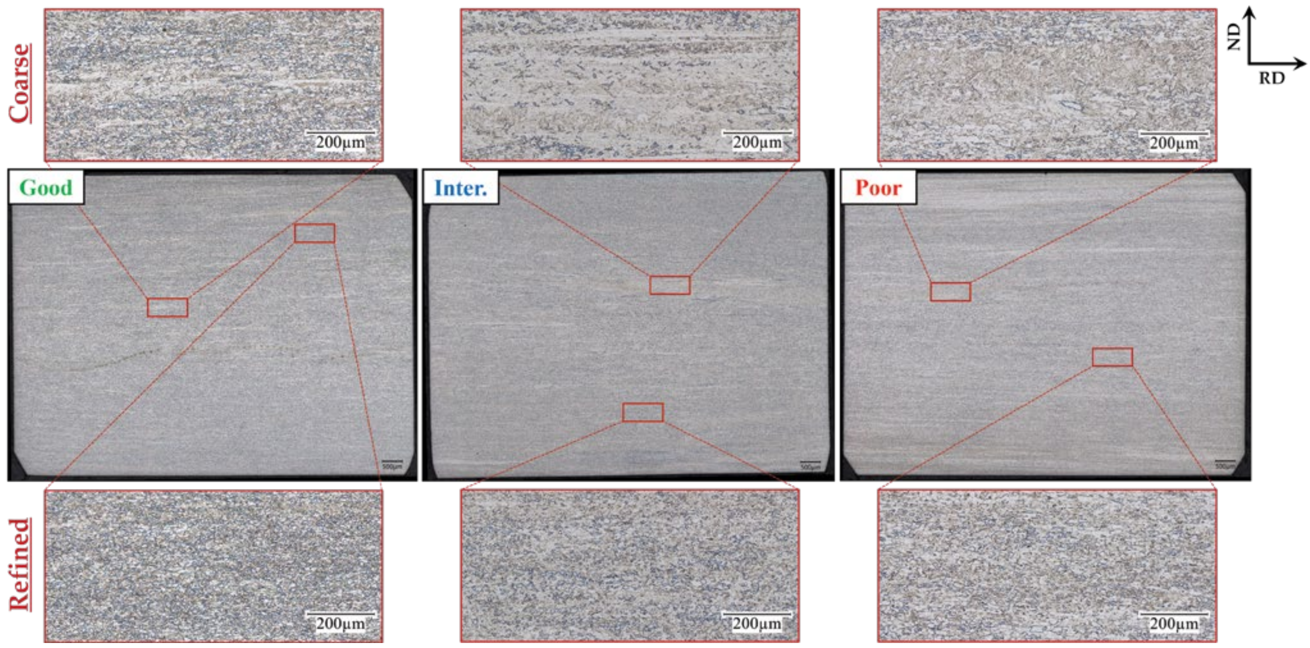

finish prior to analysis by electron backscatter diffraction (EBSD) in a scanning electron microscope. EBSD acquisition parameters included 16 mm working distance, 20 kV accelerating voltage, 300 μm × 300 μm scanned area and 0.3 μm step size. Initial tests indicated a negligible amount of austenite in the scans, so all EBSD data shown in the present study was indexed using only the α phase. EBSD analysis was performed using TSL OIM software.[21] No cleanup of the data was necessary since the scan qualities were fairly high (average confidence

Figure 7

Electron backscatter diffraction (EBSD) inverse pole figure (IPF) maps with average grain sizes (all scale bars 20 μm).

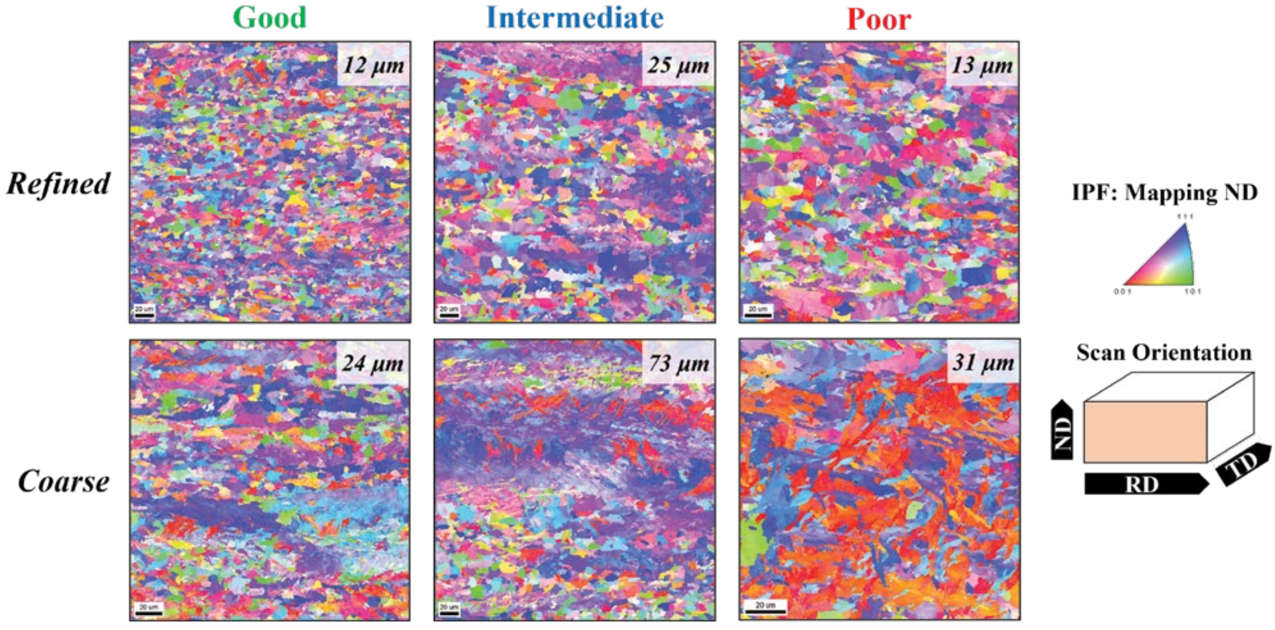

Figure 8

Cumulative area fractions versus grain orientation spread (GOS) for all three coils.

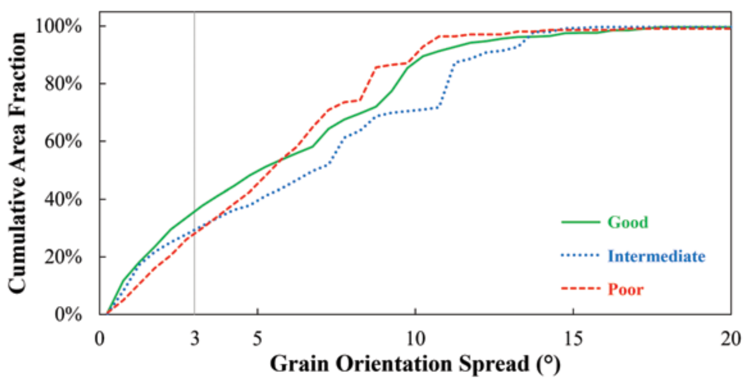

index >0.5 for all scans). Furthermore, not applying any cleanup also preserved minor spatial variations in crystallographic orientation which could otherwise have been lost. An orientation threshold of 15° was used to delimit distinct grains to maintain consistency with published literature.[3,22–25] These are treated as boundaries between effective ferrite grains, with boundary angles under 15° considered as subgrains.[26] All EBSD findings presented herein were obtained from the normal direction-rolling direction (ND-RD) plane, with the RD horizontal to the image. The crystallographic orientations at each scanned point were rotated to align the normal direction texture with the viewing direction to ensure consistency of texture analyses with published literature.[4] Scans were acquired from the refined and coarse regions of each sample, and Fig. 7 presents the resultant inverse pole figure (IPF) maps along with corresponding average grain sizes.

EBSD data analysis involved the examination of grain orientation spread (GOS) to determine recrystallized fractions. GOS is a single value assigned to each grain defined as the average deviation of all points in a grain from the average orientation of the grain. Low GOS indicates low stored lattice distortion within the grain, attributable to the relieving of stored strain energy through mechanisms such as recovery and recrystallization. Conversely, high GOS represents large amounts of stored strain energy through dislocation densities, suggesting that the effects of deformation induced during hot rolling persisted within the final product after coiling. To assess the aggregate effect of recrystallized grains, Fig. 8 shows the cumulative area fraction of microstructures vs. GOS values. Here, the y-coordinate of each point on the curve is the combined area fraction of all grains with GOS less than the x-coordinate. GOS values below 3° typically represent recrystallized grains.

Since the TMCP rolling strategy seeks austenite pancaking during latter reductions to induce fine ferrite formation upon cooling, recrystallized fractions of cooled microstructures in each coil were compared. On aggregate, the good coil showed the largest recrystallized fractions (GOS ≤3°), signifying substantial nucleation of fresh ferrite grains from deformed austenite. On the other hand, the poor coil showed the lowest recrystallized ferrite amount, with the intermediate coil slightly higher. This is indicative of a larger proportion of the poor coil retaining deformed ferrite microstructures from latter rolling stands, which is consistent with the findings from TTT comparisons showing F4–F6 occurring well past the ferrite transformation threshold.

Further microstructure examination involved texture analysis using the orientation distribution function (ODF) maps from EBSD. Fig. 9 shows the $\varphi_2 = 45°$ sections of Euler space (Bunge notation) for the ODF for each of the coils. The {001}⟨100⟩ component (triangle at top-middle) has been shown to mildly increase during warm rolling of ferrite.[27] The presence of this component in the poor coil further corroborates the TTT analysis about ferrite being rolled during latter rolling stands.

Figure 9

Representation of unrefined texture of coils using orientation distribution function (ODF) plot.

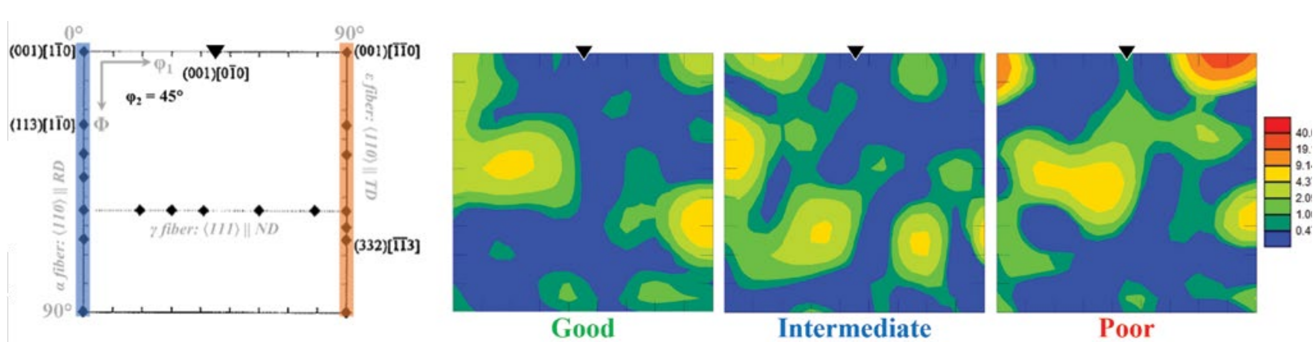

Figure 10

Fiber texture intensities for each coil to compare relative intensities of relevant texture components.

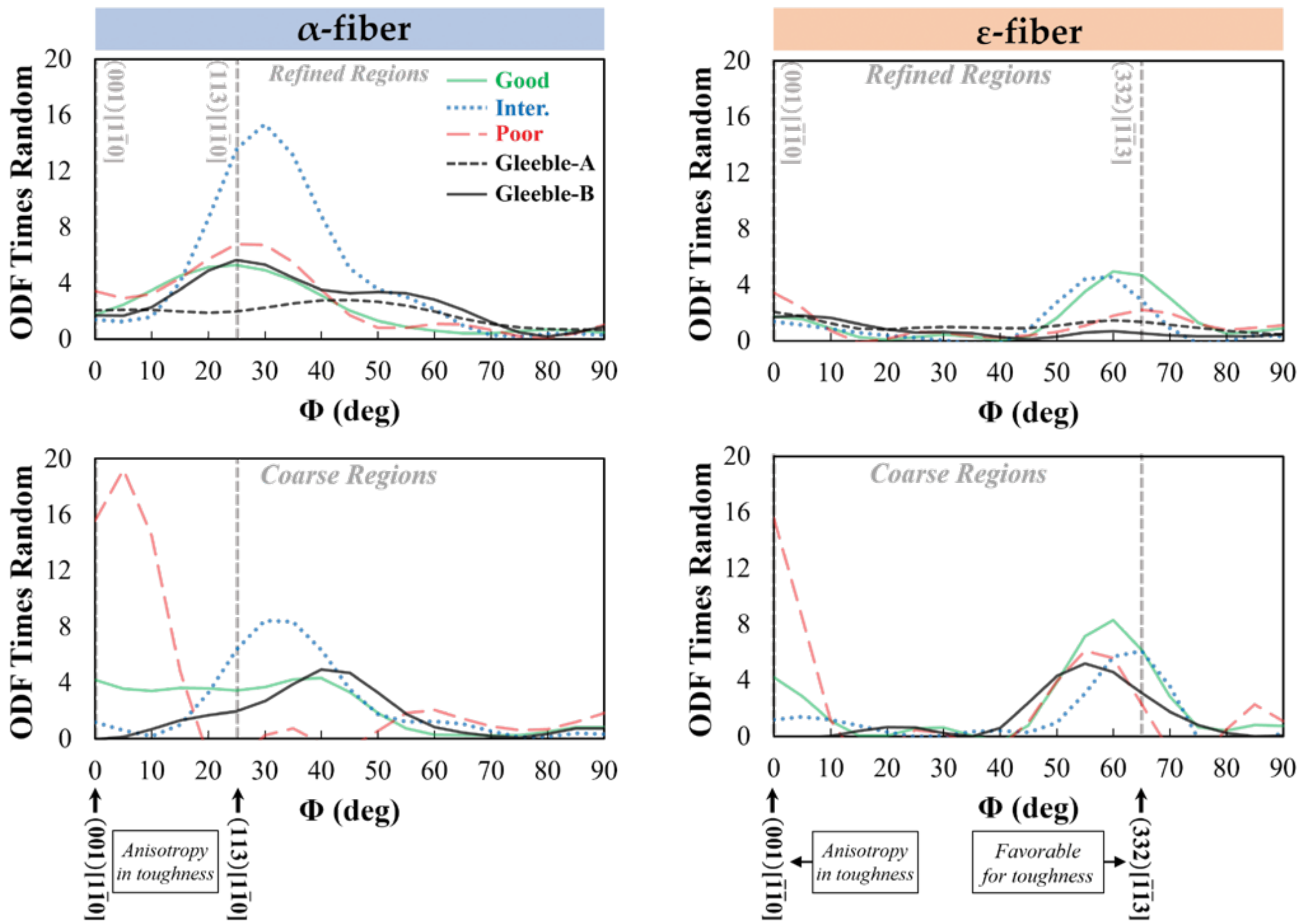

The highlighted α and ε fibers are of key importance owing to the following texture components:[4,25,28]

- Texture resulting from recrystallized austenite:
  - $(001)[1\bar{1}0]$ – anisotropic impact behavior
- Texture resulting from pancaked austenite:
  - $(332)[\bar{1}\bar{1}3]$ – favorable for impact toughness
  - $(113)[1\bar{1}0]$ – anisotropic impact behavior

Fiber plots isolated in Fig. 10 show the intensities of these texture components for each of the coils.

In the ε fiber plots, an uptick in the $(332)[\bar{1}\bar{1}3]$ texture was observed across all sets of scans, with higher prominence in the good coil. By comparison, the poor coil showed almost equivalent intensity in the coarse regions as the intermediate one but significantly lower intensity in the refined regions. For both sets of scans, the poor coil showed the strongest presence of the unfavorable $(001)[1\bar{1}0]$ component, which is highly amplified in the large unrefined regions.

In the α fiber plots, the $(001)[1\bar{1}0]$ and $(113)[1\bar{1}0]$ components are associated with anisotropic toughness behavior. Refined regions of the good and intermediate coils showed roughly equivalent intensities of the unfavorable $(001)[1\bar{1}0]$, with the poor coil being slightly higher than both. On the other hand, the unfavorable $(113)[1\bar{1}0]$ component in the intermediate sample is significantly more intense in the refined regions of the poor coil versus the good and intermediate coils. The coarse regions showed an extremely high $(001)[1\bar{1}0]$ α fiber component for the poor material, followed by the good and intermediate coils. Conversely, the order is reversed for $(113)[1\bar{1}0]$, albeit with significantly lower intensities than the unfavorable $(001)[1\bar{1}0]$ component. This shows that the good coil is not devoid of detrimental texture components, but rather the intensities of these components are far weaker than the other coils.

To summarize, while all coils showed some presence of both favorable and unfavorable texture components, the poor coil consistently showed higher intensity of unfavorable $\{001\}\langle 110\rangle$ components ($(001)[\bar{1}\bar{1}0]$ in ε and $(001)[1\bar{1}0]$ in α), which have been shown to sharpen as finishing rolling temperatures decrease.[4] On the other hand, the good coil had the highest intensity near the favorable

Figure 11

Scanning electron microscope images of fracture surfaces of Charpy impact samples depicting ductile microvoid coalescence in good and intermediate cases versus brittle cleavage in poor samples.

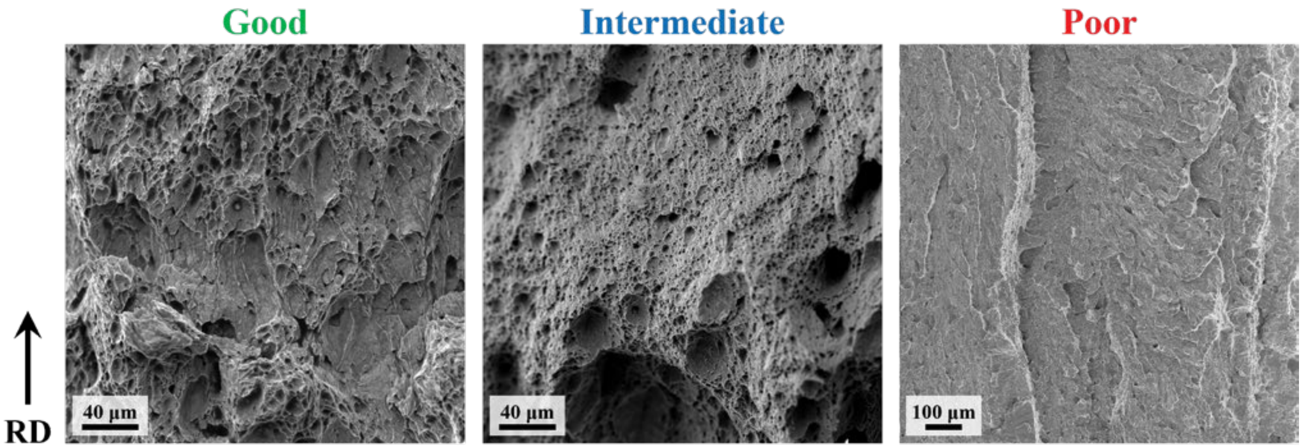

texture component for both refined and coarse portions of the microstructure. These microstructural results provide context for fractographic analysis of Charpy samples (Fig. 11). Higher-toughness samples from the good and intermediate coils exhibited microvoid coalescence, while samples from the poor coil showed prominent cleavage facets.

While crack growth in Charpy samples from all three coils is transgranular, high-angle boundaries (>15°) present greater resistance to crack propagation than low-angle boundaries, such as those inside the coarse regions.[29,30] Thus, a crack growing inside one such coarse region would encounter little resistance as it propagates from one end of the elongated grain to a high-angle boundary on the other end. With the observed coarse grains being extremely elongated (up to a few millimeters) along the same direction as crack propagation (RD), a crack growing inside the grain can easily reach the critical crack length of the material, amassing sufficient driving force (proportional to crack length) to cleave through the remaining sample material in relatively brittle fashion. Cleaved facets have been shown to occur at the same size as these effective ferrite grains.[26] The deleterious effects of coarse regions are further compounded by texture effects, since the {001}⟨110⟩ components, which were particularly high in the coarse regions of the poor coil, present favorable planes for cleavage fracture propagation.[31,32]

These findings address both observations from mechanical tests – lack of variability in tensile behavior and high variability in toughness. Unlike impact toughness tests, which are governed by crack growth, deformation during tensile testing is governed by dislocation mobility, which sees contribution from boundaries with high as well as low misorientations. Inconsistent toughness stems from the fact that the likelihood of a microcrack encountering an elongated coarse grain (inside which it can grow to critical length) is stochastic, with greater presence of coarser regions raising the probability of poor toughness.

Gleeble Hot Torsion

Simulation of Hot Rolling

To better understand the thermomechanical rolling process leading to these properties (and potentially modify them), Gleeble physical simulation was used. While multi-hit compression can be used to examine the hot rolling process, typically using flow stress or plane strain-type tests in a Gleeble Hydrawedge unit, large thickness reductions at industrial scales would render those approaches infeasible for the present study.[33,34] As such, hot torsion in a Gleeble 3500 system was used as a surrogate for hot rolling by converting the rolling profile into equivalent torsional strains and strain rates.

Sections of continuous-cast slabs of the same material as the coils were machined into torsion specimens prior to being heated and soaked to regrow and enlarge the austenite grains. After soaking, the nominal rolling profile prescribed for the coils was also applied to each torsion specimen followed by cooling at rates representative of reinforced and regular laminar cooling. Temperatures were measured using K-type thermocouples at multiple points on the gauge length to account for thermal gradient. Torsion tests were performed in a controlled atmosphere, which involved applying a vacuum to the chamber and partially backfilling with argon to minimize oxidation effects.

Deformation Control: To obtain the appropriate twist values from the nominal rolling schedule, conversions between rotation and equivalent strain (von Mises, $\overline{\varepsilon}_{eff}$) were done per Eq. 1, where r is radius of interest, θ is rotation and L is sample gauge length (20 mm).

$$\bar{\varepsilon}_{eff} = \frac{r\theta}{\sqrt{3}L}$$

(Eq. 1)

Published studies recommend an effective radius of 72.4% of the nominal radius (5 mm) to minimize effects of gradients in strain rate and strain hardening on flow curves as well as enable microstructure analysis away from the specimen surface.[35, 36] Thus, 3.62 mm was used in Eq. 1 to calculate the twist angles. Eq. 2 shows the effective shear stress (τ) for a solid circular cross-section under applied torque (T):[7, 35]

$$\tau = \frac{3T}{2\pi r^3}$$

(Eq. 2)

The corresponding equivalent stress (von Mises, $\bar{\sigma}_{eff}$) takes the form

$$\bar{\sigma}_{eff} = \frac{3\sqrt{3}T}{2\pi r^3}$$

(Eq. 3)

Rotation times were calculated from the given reduction rates. Interpass times were calculated using line speed and interstand distances assuming linear interpass cooling rates. The twist angles programmed into the Gleeble test script also included a 20° buffer to accommodate for torsion coupler free rotation, which is used to gather sufficient angular momentum before each torsion hit to minimize acceleration effects during deformation. Table 2 shows the converted Gleeble torsion schedule.

Temperature Control: Since the center of the specimen gauge section is the region of interest for microstructure examination, temperature at the center is of key interest. This presents a challenge as the amount of deformation during torsion causes detachment of the central thermocouple, requiring temperature to be controlled by a thermocouple welded at the edge of the gauge length. While the edge thermocouple is more stable, edge temperatures can be up to 50°C lower than the center. The issue is further compounded by the fact that the gradient between the edge and the center varies slightly between different thermocouple welding instances. This necessitated the development of the following new temperature control method to ensure the requisite thermal profile at the center:

i. Determine relationships to describe thermal gradient (center minus edge) as a function of temperature. Use this to define edge temperature setpoints such that center temperature coincides with target processing temperatures.

ii. Begin heating the sample, controlling with center thermocouple, at 5°C/second to target center setpoint of 1,054°C.

iii. Maintain control using the center thermocouple for the first 10 minutes of the 15-minute isothermal hold at 1,054°C. Record the edge thermocouple temperature at the end of this 10-minute period.

Table 2

Converted Temperature-Twist-Time Schedule for Gleeble Torsion

	Temperature	Reduction	Shear strain	Twist angle	Time	Interstand cooling (after rolling stand)
Initial soak	1,054°C	—	—	—	15 min.	—
F1	1,012°C	0.4118	0.713	225.8°	0.257 sec.	5.2°C/sec. for 12.50 sec.
F2	947°C	0.3394	0.588	186.1°	0.113 sec.	5.7°C/sec. for 8.21 sec.
F3	900°C	0.2710	0.469	148.6°	0.053 sec.	4.8°C/sec. for 6.04 sec.
F4	871°C	0.2350	0.407	128.8°	0.035 sec.	3.0°C/sec. for 4.62 sec.
F5	857°C	0.2016	0.349	110.5°	0.020 sec.	3.5°C/sec. for 3.69 sec.
F6	844°C	0.1445	0.250	79.2°	0.013 sec.	20.0°C/sec. for 10.50 sec. 2.7°C/sec. for 25.30 sec. (2-stage laminar cooling)

iv. Transfer control to the edge thermocouple, with an edge setpoint defined as the value recorded at the end of step iii.

v. In the act of transferring from center control to edge control, it is possible for the center to drift away from the 1,054°C isothermal hold temperature. A subroutine is defined within the program to incrementally shift the edge temperature setpoint in the correct direction to bring the center thermocouple to 1,054°C. Once the center temperature returns to 1,054°C, record the edge temperature.

vi. Subtract the hold edge temperature defined in step i from the hold edge temperature recorded at the end of step v.

vii. Shift all edge-thermocouple pass temperature setpoints defined in step i by the difference computed in step vi.

viii. Begin the cooling and torsion portions of the test with edge temperature following the values prescribed in step vii.

Torsion Testing: Figs. 12a and 12b show the overall target and measured edge temperature profiles for a rolling simulation test. The slight upticks in temperature at each pass are associated with temporary adiabatic heating brought about by rapid plastic deformation during each torsion pass. The newly proposed temperature control method did closely follow the requisite thermal profile at the center of the sample until the point where the accumulated torsional strain at the surface led to the

Figure 12

(a) Prescribed and measured temperature-time profile for edge thermocouple during Gleeble rolling simulation; (b) magnified view of "hot rolling" portion; (c) target and measured edge (control) and center temperatures. Edge thermocouple maintained appropriate sample temperatures while the center thermocouple detached around Pass 4.

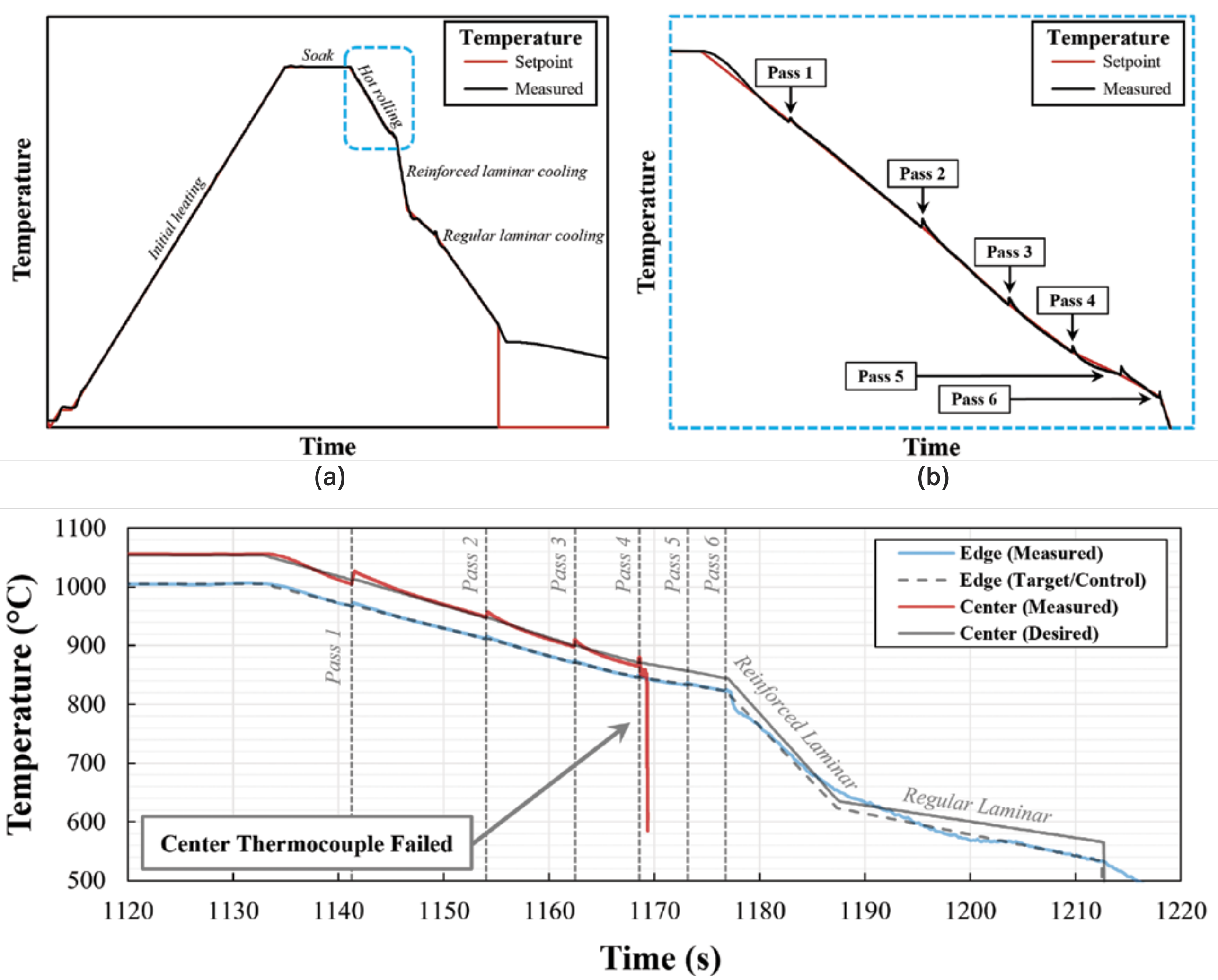

(c)

failure of the center thermocouple around the fourth pass, seen in Fig. 12c.

Microstructure Analysis: To examine the microstructure at an effective radius of 3.62 mm, the reference surface would correspond to a chord length of 6.9 mm. The target as well as sectioned reference line and plane are shown in Fig. 13. The region in the center of the 20 mm gauge length was used for EBSD examination, with the same scan size, step size and crystallographic rotation process as the coil samples. The resulting fiber texture intensities are also included in Fig. 10.

IPF maps in Fig. 14 show the microstructures after simulation of hot rolling in two selected samples (Gleeble-A and Gleeble-B). Despite being assigned identical thermomechanical profiles, Gleeble-A showed no presence of coarse microstructure anywhere on the surface. By contrast, Gleeble-B exhibited both coarse and refined regions, with average grain sizes closely matching those of the poor coil. The texture component intensities also varied slightly between the two samples. Gleeble-B showed higher intensity for the unfavorable α-fiber component in both coarse and refined regions. As for the favorable ε-fiber component, both Gleeble samples showed relatively low intensity in the refined regions, but Gleeble-B showed higher intensity in the coarse region similar to those seen in the coarse regions of all three coils.

The significant variability in microstructures produced by the same process on duplicate Gleeble samples under controlled laboratory conditions points to the fact that the particular nominal rolling parameters prescribed for large-scale production of these X65 steel coils are less tolerant of perturbations in processing parameters. A key aspect of enhancing the stability of the microstructure produced by the process is understanding the effect

Figure 13

Illustration (top) of orientation of interest for microstructure analyses from rolling and torsion. Schematic (bottom left) and optical micrograph (bottom right) depicting reference plane of Gleeble torsion specimen.

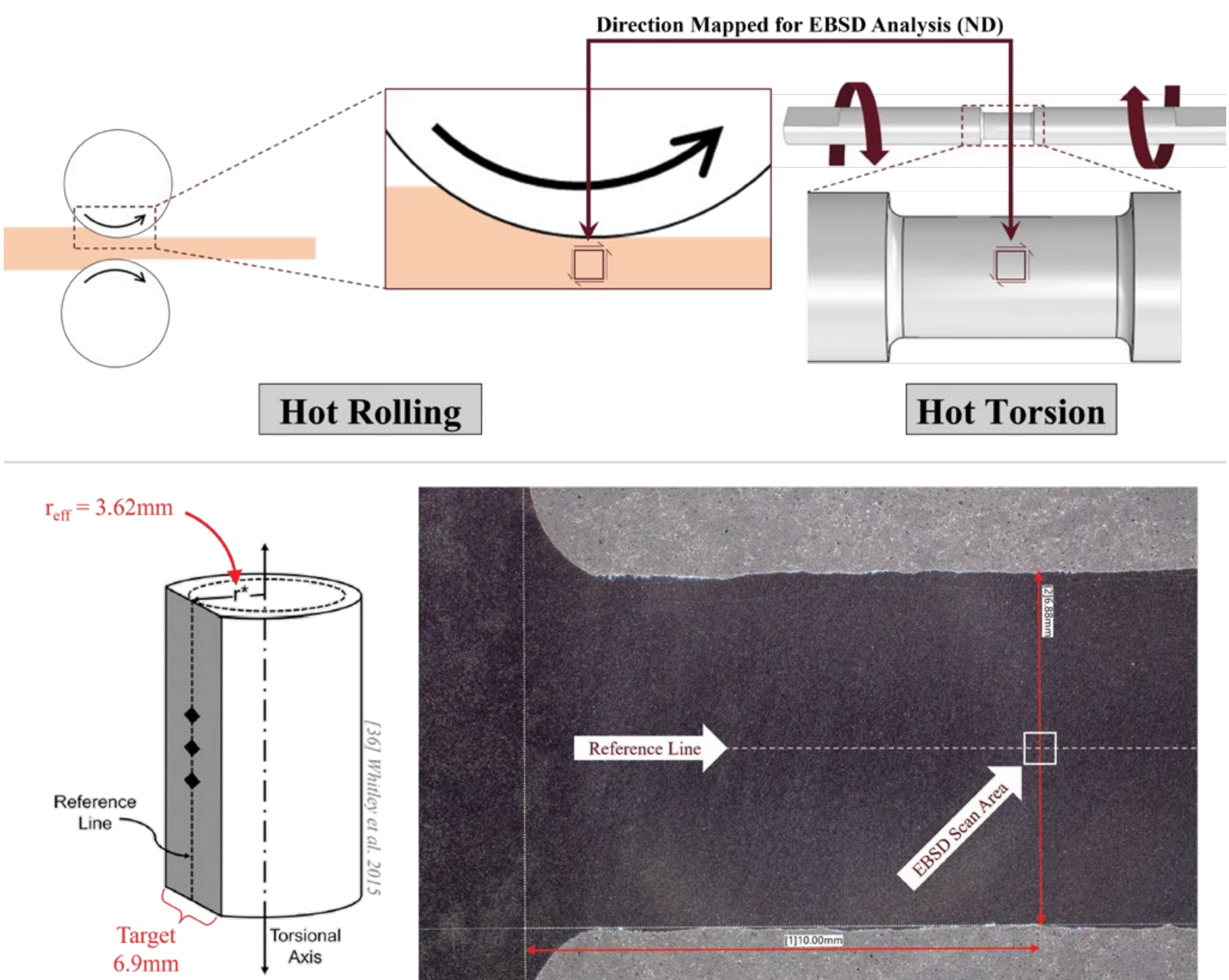

Figure 14

Inverse pole figure (IPF) maps of microstructures from Gleeble torsion simulation of hot rolling with average grain sizes. Note that Gleeble-A did not contain any coarse regions on the surface. (All scale bars are 20 µm.)

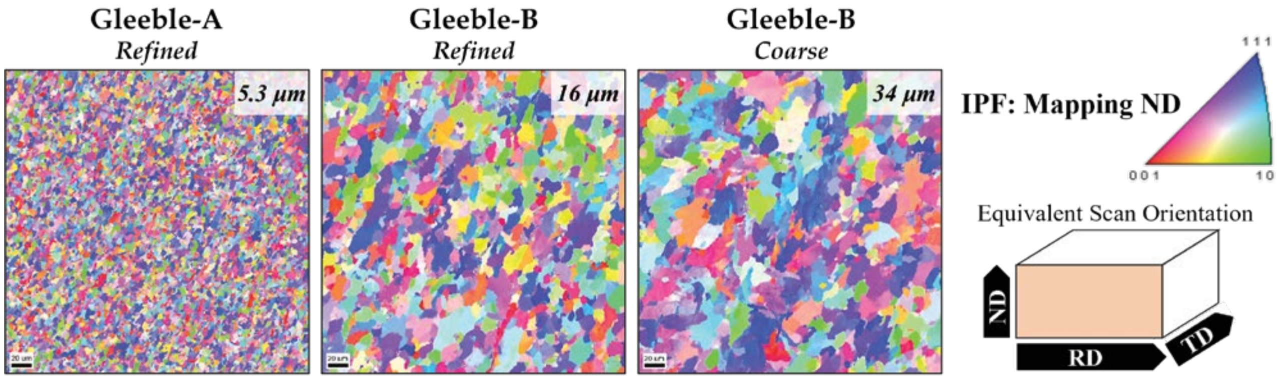

of stand temperatures, processing time (particularly through line speed) and reductions at each stand on austenite recrystallization activity.

Double-Twist Testing for Recrystallization

Given the importance of austenite recrystallization to the final microstructure, and consequently impact toughness, Gleeble double-twist testing was used to establish temperature windows for full and partial recrystallization. Double-twist testing combines notions of double-hit compression and multistep hot torsion, allowing for multiple methods of estimating recrystallization temperatures within a single test.[37] The method provides the benefits of higher accumulated strain to capture effects of prior deformation as well as successive hits at each temperature for fractional softening measurement.

Torsion samples machined from sections of continuous-cast slabs were soaked at 1,200°C prior to applying two isothermal deformation hits with a 5 second interhit time. Next, the samples were cooled by 50°C at 2.5°C/second before repeating the isothermal deformation hits. These 50°C descending steps were repeated until 750°C. Fig. 15 shows the equivalent stress-strain data.

Fig. 16 illustrates two methods of estimating recrystallization thresholds from double-twist data. Fractional softening (FS), defined as change in mean flow stress between successive hits, was used to estimate full recrystallization (T_r, FS > 0.8) and nil recrystallization (T_{nr}, FS < 0.2) temperatures (Fig. 16a), with the window between both being the partial recrystallization range.[38] In addition, mean flow stresses of first hits at each temperature were plotted against inverse absolute temperature, with the inflection point representing the nil recrystallization temperature (Fig. 16b).[37] The increase in softening after pass 15 corresponds to deformation in the α-γ intercritical range, since these passes occur close to the equilibrium A_3 temperature.[10]

Figure 15

Equivalent stress-strain output of double-twist testing over a range of temperatures.

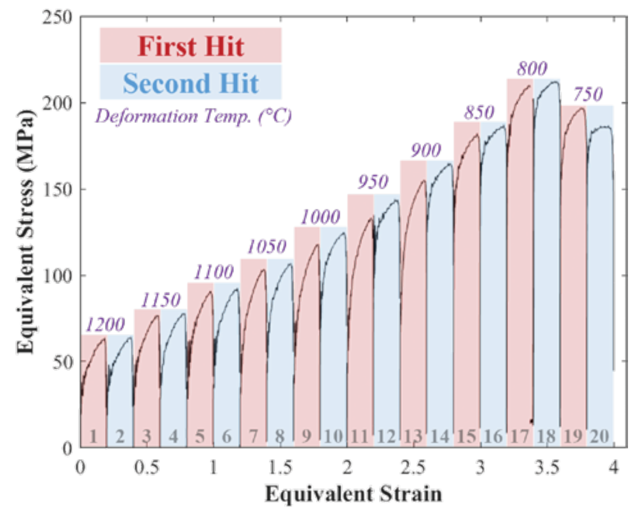

Two different soak durations (15 minutes, 1 hour) at 1,200°C were examined to ensure austenitic grains were sufficiently enlarged prior to double-twist testing (20% strain per hit). Prolonging the soak time had negligible effect on T_r, with averages of 1079°C (±31°C) and 1077°C (±38°C) for 15-minute and 1-hour holds per the FS method. Both methods of estimating T_{nr} yielded consistent results with values of 938°C (±32°C) using FS and 937°C (±20°C) using inverse absolute temperature.

In addition to baseline 20% strain per hit, 40% strain per hit was also tested to assess the effect of deformation amount on recrystallization thresholds (15-minute soak at 1,200°C). As expected, the larger strains allowed recrystallization to persist until much lower temperatures,

Figure 16

Estimation of recrystallization threshold temperatures using fractional softening (a) and inverse temperature (b).

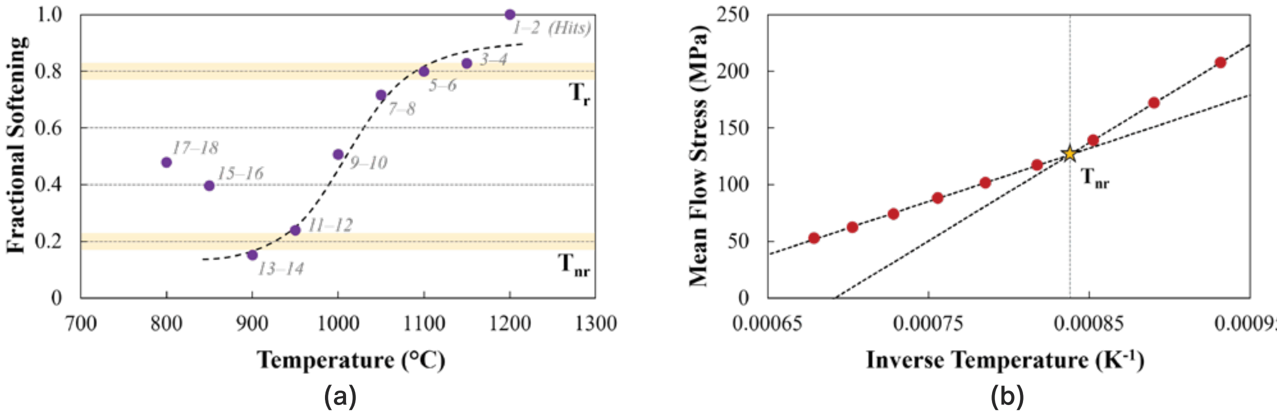

with 40% strain per hit leading to a T_r of 942°C and a combined T_{nr} estimate of 859°C (±38°C).

The target TMCP rolling strategy involves initial reductions (F1, F2) above T_r for austenite recrystallization followed by latter reductions (F3–F6) below T_{nr} for austenite pancaking, avoiding the partial recrystallization window between T_r and T_{nr}. The presented findings, however, suggest that some reductions, particularly F2–F4 (for all three coils), did occur in this partial recrystallization range, leading to inconsistent deformation and recrystallization behavior, and consequently inconsistent impact toughness.

Effect of Prior Deformation History on Recrystallization

Since recrystallization depends on the amount of deformation (in addition to temperature, time, and deformation rate), rolling simulation and double-twist testing were combined to study the effect of prior hot rolling history on subsequent recrystallization thresholds. The steps to examine the effects for a particular rolling stand of interest were:

i. Apply thermomechanical profile prior to stand of interest.

ii. Simulate reduction and temperature at stand of interest.

iii. Hold temperature for interpass time after stand exit, then reapply the same strain and strain rate as step ii.

iv. Cool by 50°C and perform two torsion hits using same strains and interhit time as step iii.

v. Repeat step iv until below 750°C.

A schematic depicting the process with F3 as the stand of interest is shown in Fig. 17. This process was applied to simulate prior history on each of the six stands, and the resultant partial recrystallization thresholds (T_r) were determined by the FS method.

T_r values due to accumulated deformation after F1, F2, F3 and F4 were found to be 886°C, 929°C, 885°C and 850°C, respectively. T_r could not be established after the last two stands due to no discernible recrystallization. While accounting for prior rolling histories at each stand did shift the exact T_r threshold values, the findings remain consistent with the inferences from double-twist testing regarding deformations at the intermediate stands occurring in the partial recrystallization range.

Conclusions

The present study examined three similarly produced Nb+V+Ti X65 steel coils exhibiting inconsistent Charpy impact behavior (good, intermediate and poor toughness). The coils were industrially produced by TMCP hot rolling through six stands (F1–F6) with the strategy of recrystallizing austenite in the initial passes and pancaking austenite in the latter passes to induce transformation into refined ferrite upon cooling.

Figure 17

Example schematic of combined rolling simulation and double-twist testing to study effects of prior reductions on recrystallization behavior. In this example, the effects of F1 and F2 on F3 recrystallization are being examined.

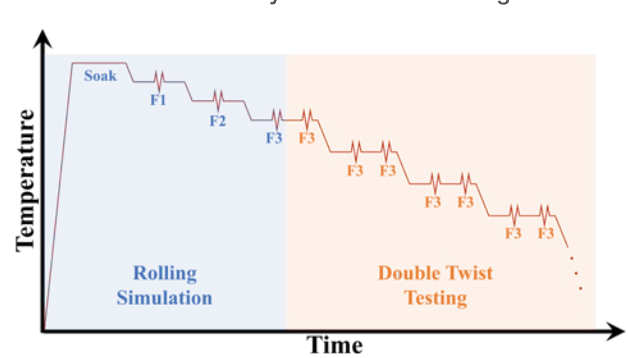

- Samples tested from all three coils showed no meaningful difference in chemical composition, quasi-static tension metrics and high-strain-rate mechanical behavior.
- Examination of production logs of the coils revealed discrepancies in their processing histories.
  - The good coil had the shortest processing time, while the poor coil had the slowest processing time and lowest stand temperatures. The intermediate coil had similar stand temperatures as the good coil but similar processing time as the poor coil.
  - Overlaying the time-temperature profiles of each coil with TTT diagrams showed that performing rolling reductions farther into the transformed ferrite regions led to worse impact behavior.
- Microstructure analysis was used to shed more light on the effects of processing parameters.
  - Optical metallography revealed mixed microstructures with refined and large coarse regions suggesting inconsistent recrystallization during hot rolling.
  - In-depth EBSD analysis of recrystallized fractions (using GOS) and fiber texture components followed the same trends as impact toughness.
- Gleeble thermomechanical simulation was used to precisely manipulate processing parameters.
  - Hot torsion was performed as a surrogate for hot rolling to replicate industrial rolling parameters. Identically controlled Gleeble samples showed very different microstructures, with fully refined grains in some cases and mixed (coarse + refined) grains similar to the rolled coils in other cases, pointing to a lack of stability in microstructures resulting from the prescribed nominal rolling parameters.
  - Double-twist torsion tests at multiple temperatures and strain levels were used to estimate partial (T_r) and nil recrystallization (T_{nr}) thresholds in order to determine thermal ranges to target (and avoid) for austenite recrystallization and pancaking during TMCP.
  - A combined approach consisting of hot rolling simulation followed by double-twist torsion was used to assess the effects of prior rolling history on partial recrystallization thresholds.

Findings from the examination of processing histories, microstructure analyses, and multiple Gleeble physical simulation approaches all support the inference that some hot rolling passes occurred in the partial recrystallization window between T_r and T_{nr}. Microstructures resulting from processing in this window show extreme sensitivity to perturbations in processing, leading to inconsistent recrystallization, and therefore inconsistent impact toughness.

Acknowledgments

The authors express their gratitude to Steel Dynamics Inc. – Flat Roll Group personnel at the Columbus and Southwest-Sinton divisions for technical and material support toward the completion of this work. The authors also extend thanks to the leadership and staff at the Center for Advanced Vehicular Systems, particularly Clayton Walden and Michael Newman, the Institute for Imaging and Analytical Technologies, and the Michael W. Hall School of Mechanical Engineering at Mississippi State University for their research infrastructure and technical expertise.

This article is available online at AIST.org for 30 days following publication.

References

1. K. Nishioka and K. Ichikawa, "Progress in Thermomechanical Control of Steel Plates and Their Commercialization," *Science and Technology of Advanced Materials,* Vol. 13, No. 2, 2012, p. 023001.
2. P. Hurley, B.C. Muddle and P.D. Hodgson, "Nucleation Sites for Ultrafine Ferrite Produced by Deformation of Austenite During Single-Pass Strip Rolling," *Metallurgical and Materials Transactions A,* Vol. 32, No. 6, 2001, pp. 1507–1517.
3. R. Shukla, S.K. Das, B. Ravi Kumar, S.K. Ghosh, S. Kundu and S. Chatterjee, "An Ultra-low Carbon, Thermomechanically Controlled Processed Microalloyed Steel: Microstructure and Mechanical Properties," *Metall Mater Trans A,* Vol. 43, No. 12, December 2012, pp. 4835–4845, https://doi.org/10.1007/s11661-012-1273-7.
4. R.K. Ray, J.J. Jonas, M.P. Butrón-Guillén and J. Savoie, "Transformation Textures in Steels," *ISIJ International,* Vol. 34, No. 12, 1994, pp. 927–942, https://doi.org/10.2355/isijinternational.34.927.
5. F.J. Humphreys and M. Hatherly, *Recrystallization and Related Annealing Phenomena,* 2nd ed., Elsevier, Amsterdam, The Netherlands; Boston, Mass., USA, 2004.
6. D. Raabe, "Recovery and Recrystallization: Phenomena, Physics, Models, Simulation," *Physical Metallurgy,* Elsevier, 2014, pp. 2291–2397, https://doi.org/10.1016/B978-0-444-53770-6.00023-X.
7. G.E. Dieter, *Mechanical Metallurgy,* 3rd ed., McGraw-Hill, New York, N.Y., USA, 1986.
8. F.H. Samuel, S. Yue, J.J. Jonas and B.A. Zbinden, "Modeling of Flow Stress and Rolling Load of a Hot Strip Mill by Torsion Testing," *ISIJ International,* Vol. 29, No. 10, 1989, pp. 878–886, https://doi.org/10.2355/isijinternational.29.878.
9. N. Nakata and M. Militzer, "Modelling of Microstructure Evolution During Hot Rolling of a 780 MPa High Strength Steel," *ISIJ Int.,* Vol. 45, No. 1, 2005, pp. 82–90, https://doi.org/10.2355/isijinternational.45.82.

10. J. Calvo, L. Collins and S. Yue, "Design of Microalloyed Steel Hot Rolling Schedules by Torsion Testing: Average Schedule vs. Real Schedule," *ISIJ international,* Vol. 50, No. 8, 2010, pp. 1193–1199.
11. F. Siciliano, "High-Strength Line Pipe Steels and Physical Simulation of Production Processes," *Advanced High Strength Steel: Processing and Applications,* Springer, 2018, pp. 71–78.
12. "Gleeble Thermal-Mechanical Simulators," Gleeble, accessed 9 December 2021, www.gleeble.com.
13. "Thermo-Calc Software TCFE9 Steels/Fe-alloys Database," ThermoCalc, accessed 24 January 2022, https://thermocalc.com/products/databases/steel-and-fe-alloys.
14. V. Tvergaard and A. Needleman, "Effect of Material Rate Sensitivity on Failure Modes in the Charpy V-Notch Test," *Journal of the Mechanics and Physics of Solids,* Vol. 34, No. 3, January 1986, pp. 213–241, https://doi.org/10.1016/0022-5096(86)90019-0.
15. A. Rossoll, C. Berdin, P. Forget, C. Prioul and B. Marini, "Mechanical Aspects of the Charpy Impact Test," *Nuclear Engineering and Design,* Vol. 188, No. 2, April 1999, pp. 217–229, https://doi.org/10.1016/S0029-5493(99)00017-5.
16. E. Lucon, "Experimental Assessment of the Equivalent Strain Rate for an Instrumented Charpy Test," *J. Res. Natl. Inst. Stan.,* Vol. 121, April 2016, p. 165, https://doi.org/10.6028/jres.121.007.
17. N. Saunders, U.K.Z. Guo, X. Li, A.P. Miodownik and J.-P. Schillé, "Using JMatPro to Model Materials Properties and Behavior," *JOM*, Vol. 55, No. 12, December 2003, pp. 60–65, https://doi.org/10.1007/s11837-003-0013-2.
18. E.M. Focht, "Static Recrystallization Behavior of Austenite in HSLA 100 During Thermomechanical Controlled Processing (TMCP)," Defense Technical Information Center, November 1994. https://doi.org/10.21236/ADA288737.
19. S.J. Wu and C.L. Davis, "Effect of Duplex Ferrite Grain Size Distribution on Local Fracture Stresses of Nb-Microalloyed Steels," *Materials Science and Engineering: A,* Vol. 387–389, December 2004, pp. 456–460, https://doi.org/10.1016/j.msea.2004.01.144.
20. D. Chakrabarti, "Development of Bimodal Grain Structures and Their Effect on Toughness in HSLA Steel," Ph.D. thesis, University of Birmingham, 2007.
21. "EDAX OIM Analysis," EDAX, https://www.edax.com/products/ebsd/oim-analysis.
22. M. Díaz-Fuentes, A. Iza-Mendia and I. Gutiérrez, "Analysis of Different Acicular Ferrite Microstructures in Low-Carbon Steels by Electron Backscattered Diffraction. Study of Their Toughness Behavior," *Metall and Mat Trans A,* Vol. 34, No. 11, November 2003, pp. 2505–2516, https://doi.org/10.1007/s11661-003-0010-7.
23. B. Hwang, Y.G. Kim, S. Lee, Y.M. Kim, N.J. Kim and J.Y. Yoo, "Effective Grain Size and Charpy Impact Properties of High-Toughness X70 Pipeline Steels," *Metall and Mat Trans A,* Vol. 36, No. 8, August 2005, pp. 2107–2114, https://doi.org/10.1007/s11661-005-0331-9.
24. S.Y. Shin, B. Hwang, S. Lee, N.J. Kim and S.S. Ahn, "Correlation of Microstructure and Charpy Impact Properties in API X70 and X80 Line-Pipe Steels," *Materials Science and Engineering: A*, Vol. 458, No. 1–2, June 2007, pp. 281–289, https://doi.org/10.1016/j.msea.2006.12.097.
25. S. Nafisi, M.A. Arafin, L. Collins and J. Szpunar, "Texture and Mechanical Properties of API X100 Steel Manufactured Under Various Thermomechanical Cycles," *Materials Science and Engineering: A,* Vol. 531, January 2012, pp. 2–11, https://doi.org/10.1016/j.msea.2011.09.072.
26. A. Ghosh, S. Sahoo, M. Ghosh, R.N. Ghosh and D. Chakrabarti, "Effect of Microstructural Parameters, Microtexture and Matrix Strain on the Charpy Impact Properties of Low Carbon HSLA Steel Containing MnS Inclusions," *Materials Science and Engineering: A,* Vol. 613, September 2014, pp. 37–47, https://doi.org/10.1016/j.msea.2014.06.091.
27. P.P. Bhattacharjee, M. Zaid, G.D. Sathiaraj and B. Bhadak, "Evolution of Microstructure and Texture During Warm Rolling of a Duplex Steel," *Metall Mater Trans A,* Vol. 45, No. 4, April 2014, pp. 2180–2191, https://doi.org/10.1007/s11661-013-2139-3.
28. M.P. Butrón-Guillén, J.J. Jonas and R.K. Ray, "Effect of Austenite Pancaking on Texture Formation in a Plain Carbon and a Nb Microalloyed Steel," *Acta Metallurgica et Materialia,* Vol. 42, No. 11, November 1994, pp. 3615–3627, https://doi.org/10.1016/0956-7151(94)90428-6.
29. M.E. Natishan, "Mechanisms of Strength and Toughness in a Microalloyed, Precipitation Hardened Steel," David Taylor Research Center, SME-88-81, April 1989, https://apps.dtic.mil/sti/tr/pdf/ADA210571.pdf.
30. E. Smith, "The Nucleation and Growth of Cleavage Microcracks in Mild Steel," *Proceedings of Physical Basis of Yield and Fracture,* Physical Society of Oxford, 1966, pp. 30–46.
31. Y. Tian, H.T. Wang, Q.B. Ye, Q.H. Wang, Z.D. Wang and G.D. Wang, "Effect of Rolling Reduction Below γ Non-Recrystallization Temperature on Pancaked γ, Microstructure, Texture and Low-Temperature Toughness for Hot Rolled Steel," *Materials Science and Engineering: A,* Vol. 794, September 2020, p. 139640, https://doi.org/10.1016/j.msea.2020.139640.
32. E. Bouyne, H.M. Flower, T.C. Lindley and A. Pineau, "Use of EBSD technique to examine microstructure and cracking in a bainitic steel," *Scripta Materialia,* Vol. 39, No. 3, July 1998, pp. 295–300, https://doi.org/10.1016/S1359-6462(98)00170-5.
33. S. T. Mandziej, "Physical Simulation of Metallurgical Processes," *Materials and Technology,* Vol. 44, No. 3, 2010, pp. 105–119.
34. T. Lillo, J. Simpson, and J. Walleser, "Summary of Gleeble-Based, High Temperature Deformation Study on AF9628 Steel," 2019.
35. D. Barraclough, H. Whittaker, K. Nair, and C. Sellars, "Effect of Specimen Geometry on Hot Torsion Test Results for Solid and Tubular Specimens," *J. Test. Eval.,* Vol. 1, No. 3, 1973, pp. 220–226, https://doi.org/10.1520/JTE10007J.
36. B.M. Whitley, A.L. Araujo, J.G. Speer, K.O. Findley and D.K. Matlock, "Analysis of Microstructure in Hot Torsion Simulation," *Matls. Perf. Charact.,* Vol. 4, No. 3, November 2015, pp. 307–321, https://doi.org/10.1520/MPC20150012.
37. T.J. Ballard, J.G. Speer, K.O. Findley and E. De Moor, "Double-Twist Torsion Testing to Determine the Non Recrystallization Temperature," *Sci Rep,* Vol. 11, No. 1, January 2021, p. 1495, https://doi.org/10.1038/s41598-021-81139-1.
38. A.I. Fernández, B. López and J.M. Rodríguez-Ibabe, "Relationship Between the Austenite Recrystallized Fraction and the Softening Measured From the Interrupted Torsion Test Technique," *Scripta Materialia,* Vol. 40, No. 5, February 1999, pp. 543–549, https://doi.org/10.1016/S1359-6462(98)00452-7.

This paper was presented at AISTech 2026 — The Iron & Steel Technology Conference and Exposition, Pittsburgh, Pa., USA, and published in the AISTech 2026 Conference Proceedings.